



# **JGR Space Physics**

# RESEARCH ARTICLE

10.1029/2021JA029657

#### **Key Points:**

- Observations by RISR-N reveal a co-mingling of cold patches and a transpolar arc, creating a region of elevated Ne and Te ("hot patch")
- The combination of transport and soft precipitation is a signature of lobe reconnection and suggests a new mechanism for hot patch generation
- Numerical modeling of the event predicts an enhancement in Ne and Te at DMSP altitudes due to diffusion, not the presence of a patch

#### **Supporting Information:**

Supporting Information may be found in the online version of this article.

#### Correspondence to:

J. Díaz Peña, jmdp@bu.edu

#### Citation:

Díaz Peña, J., Semeter, J., Nishimura, Y., Varney, R., Reimer, A., Hairston, M., et al. (2021). Auroral heating of plasma patches due to high-latitude reconnection. *Journal of Geophysical Research: Space Physics*, *126*, e2021JA029657. https://doi.org/10.1029/2021JA029657

Received 11 JUN 2021 Accepted 12 NOV 2021

# **Author Contributions:**

Conceptualization: Joaquín Díaz Peña, Joshua Semeter

**Data curation:** Yukitoshi Nishimura, Roger Varney, Ashton Reimer, Marc Hairston, Michael Hirsch

Formal analysis: Joaquín Díaz Peña, Joshua Semeter, Marc Hairston, Matthew Zettergren

Funding acquisition: Olga Verkhoglyadova

Investigation: Joaquín Díaz Peña Methodology: Joaquín Díaz Peña, Roger

**Resources:** Roger Varney, Ashton Reimer, Marc Hairston, Keisuke Hosokawa

Software: Joaquín Díaz Peña, Matthew Zettergren, Michael Hirsch Supervision: Joshua Semeter, Olga Verkhoglyadova

© 2021. American Geophysical Union. All Rights Reserved.

# **Auroral Heating of Plasma Patches Due to High-Latitude Reconnection**

Joaquín Díaz Peña¹ D, Joshua Semeter¹ D, Yukitoshi Nishimura¹ D, Roger Varney² D, Ashton Reimer² D, Marc Hairston³ D, Matthew Zettergren⁴ D, Michael Hirsch¹ D, Olga Verkhoglyadova⁵ D, Keisuke Hosokawa⁴ D, and Kazuo Shiokawa² D

<sup>1</sup>Department of Electrical Engineering and Center for Space Physics, Boston University, Bosto, MA, USA, <sup>2</sup>SRI International, Menlo Park, CA, USA, <sup>3</sup>William B. Hanson Center for Space Sciences, The University of Texas at Dallas, Dallas, TX, USA, <sup>4</sup>Embry-Riddle Aeronautical University, Daytona Beach, FL, USA, <sup>5</sup>Jet Propulsion Laboratory, California Institute of Technology, Pasadena, CA, USA, <sup>6</sup>Department of Communication Engineering and Informatics, The University of Electro-Communications, Chofu, Japan, <sup>7</sup>Institute for Space-Earth Environmental Research, Nagoya University, Nagoya, Japan

**Abstract** This study exploits the volumetric sampling capabilities of the Resolute Bay Incoherent Scatter Radar (RISR-N) in collaboration with all-sky imagery and in situ measurements to examine the interplay between cold plasma transport and auroral precipitation during a high-latitude lobe reconnection event on the dawn side. Solar wind IMF preceding the event was characterized by an impulsive negative excursion in B. embedded within a period of  $B_z > 0$  and  $B_y < 0$ . The combined effects of transport and magnetic stress release associated with a high-latitude reconnection pulse drove a co-mingling between patches and soft electron precipitation, creating common regions of elevated electron density and temperature. Vertical ionospheric profiles extracted in the rest frame of the drifting patch showed a contemporaneous increase in T<sub>a</sub> above 200 km and N<sub>a</sub> below 250 km while at the same time showing only a small impact in N<sub>a</sub> near the F-region peak. The observations suggest a new mechanism for creating a "hot patch" wherein the density enhancement is not generated by the precipitation but is warmed by it. The physics-based GEMINI model was used to explore the response to the observed precipitation as a function of altitude and time. Model results suggest that a correlated enhancement in  $N_a$  and  $T_a$  at DMSP altitudes (~800 km), that is, hot patch, can be produced by auroral heating and upward diffusion, irrespective of lower altitude density structure. The study highlights the need for densely distributed observations in space and time for understanding both mesoscale and small-scale ionospheric dynamics in regions subject to complex forcing.

#### 1. Introduction

Magnetic reconnection represents a fundamental mode of energy transfer into and out of the geospace system. Many phenomena of the polar ionosphere may be directly traced to reconnection, including the formation of fast flow channels (Zou et al., 2015), poleward moving auroral forms (Oksavik et al., 2004), poleward boundary intensifications (PBI's) along the nightside separatrix (De la Beaujardiere et al., 1994; Zou et al., 2016), and ionospheric upflow in the cusp (Strangeway et al., 2000) and nightside auroral regions (Semeter et al., 2003). From an energy perspective, the merging of the solar wind and magnetosphere constitutes a magnetospheric generator, establishing the electric fields that drive complex convection patterns in the ionosphere. For periods of southward interplanetary magnetic field (IMF), observational evidence suggests that, on average, there is a balance between magnetopause reconnection on the dayside and magnetotail reconnection on the nightside (Dungey, 1961). When the IMF is northward directed, reconnection occurs differently from the southward IMF. Regions that are favorable to reconnection shift from the dayside magnetopause to the lobe magnetic field lines poleward of the cusps (Gosling et al., 1991). The formation of reverse convection cells, multi-cell convection patterns, and soft discrete arcs in the polar cap are some of the consequences that arise due to the reversal in orientation of the IMF  $B_z$  component from negative (southward) to positive (northward) (Fuselier et al., 2000; Lockwood & Moen, 1999; Øieroset et al., 1997; Onsager et al., 2001).

Ground-based observations have shown that reconnection is not a continuous smooth process, and the existence of reconnection pulses is expected regardless of the IMF orientation (Fear et al., 2017). For southward IMF conditions, pulsed reconnection on the dayside is one of the major agents for the creation of F-region plasma patches (or polar cap patches) (Crowley, 1996; Tsunoda, 1988). Patches are enhanced density regions that are generated



Validation: Joshua Semeter, Yukitoshi Nishimura, Roger Varney, Ashton Reimer, Marc Hairston, Michael Hirsch, Olga Verkhoglyadova, Keisuke Hosokawa Visualization: Joaquín Díaz Peña, Michael Hirsch Writing – original draft: Joaquín Díaz Peña, Joshua Semeter Writing – review & editing: Joaquín Díaz Peña, Joshua Semeter in the dayside and convected across the polar cap toward the night side, with reconnection serving as the trigger for patch generation and segmentation (Basu & Valladares, 1999; Carlson, 1994, 2007, 2012; Lockwood & Carlson, 1992). The regions of higher plasma density drift and deform in a manner consistent with general convection streamlines established by electrostatic potential contours. For northward IMF, polar cap patches are still expected (Coley & Heelis, 1998; McEwen & Harris, 1996; Zhang et al., 2016), particularly if there are sudden changes of  $B_z$  (Valladares et al., 1998) and in the presence of precipitation (Oksavik et al., 2006). In general, the solar wind does not smoothly vary, and rapid transients in IMF can impart rapid reconfigurations of convective flows in the ionosphere (Lu et al., 2002; Ruohoniemi & Greenwald, 1998).

This article presents a detailed examination of plasma transport, auroral ionization, and auroral heating associated with a southward transient in the solar wind IMF embedded within a prolonged period of northward IMF. Observations by the electronically scannable Resolute Bay Incoherent Scatter Radar (RISR-N) and the co-located Optical Mesosphere Thermosphere Imager (OMTI) have revealed a coordinated response, wherein a plasma patch was observed to accelerate into a region of an intensifying sun-aligned arc. The co-mingling of the patch and soft precipitation created a common region of elevated ionospheric density and elevated electron temperature consistent with the designation "hot patch" (Zhang et al., 2017). The formation of convection transients and soft structured precipitation are expected consequences of magnetic stress release due to lobe reconnection, as discussed in previous works (Milan et al., 2005).

The key observational innovation in this work is the use of the pulse-by-pulse steering capability of RISR-N to construct time-dependent volumetric images of the ionosphere in the vicinity of the auroral forms. This enables us to track plasma structures and to explore the relative importance of recombination, diffusion, heating, and impact ionization in the patch (Lagrangian) reference frame. The observations are used to constrain the first-principles GEMINI numerical model to elucidate the relationship between F-region parameters observed by RISR and topside (800 km) parameters measured by Defense Meteorological Satellite Program (DMSP). The latter has served as the basis for recent work on plasma patch dynamics (Ma et al., 2018; Zhang et al., 2017).

# 2. Instruments and Setting

The case study examined in this work occurred on January 24, 2012. This period was selected based on the fortuitous availability of concurrent measurements by DMSP, the OMTI auroral imager, and the RISR-N facility during an extended interval where the open-closed field-line boundary was observed by all diagnostics. For context, Figure 1 summarizes the solar wind magnetic field measured at L1. The data were obtained from the NASA/GSFC's OMNI data set through OMNIWeb, and have been time-shifted to the Earth's bow shock. The transfer time to the ionosphere from this point depends on factors such as the IMF orientation and the mode of magnetosphere-ionosphere coupling (Ruohoniemi & Greenwald, 1998; Watanabe et al., 2005), but is expected to be of order a few minutes. The period beginning at  $\sim$ 9:45 UT was characterized by a steady IMF  $B_z$  positive and  $B_y$  negative-conditions favorable for a contracted auroral oval and high-latitude reconnection (Milan et al., 2005). An exception was a sharp dip and sign reversal in  $B_z$  at  $\sim$ 11:15 UT. It has been shown that even a brief interval of enhanced dayside merging can lead to a substantial re-inflation of the polar cap (Newell et al., 1997) and the creation of new polar cap patches (Valladares et al., 1998). This dynamic is considered significant for understanding the regional dynamics of interest to this study.

#### 2.1. **RISR-N**

The RISR-N facility (74.73°N, 94.91°W) provided the crucial spatially and temporally resolved data for this study. During the period of interest, RISR-N cycled through the 42 beam pattern depicted in a radar-centered horizontal coordinate system in Figure 2a. Beam-patterns such as this enable the construction of three-dimensional volumetric images of density  $N_e$ , electron temperature  $T_e$ , ion temperature  $T_i$ , and line-of-site ion velocity  $V_{LOS}$ . The uncertainties in observed state parameters depend on the number of samples integrated per position and the backscattered power, which decreases with ionospheric density and range (Davis & McCrea, 2004; Farley, 1969). For this experiment, we used a 2 min integration period, corresponding to 171 pulses per beam position.

Figure 2b shows an example of the sampled density field, with each sample displayed as a color-coded dots. Note that the cross-range sample spacing increases with increasing altitude, with horizontal coverage increasing from  $\sim 200 \times 200$  km at E-region altitudes to  $\sim 400 \times 400$  km near the F-region peak. The fitted data are typically

DÍAZ PEÑA ET AL. 2 of 17



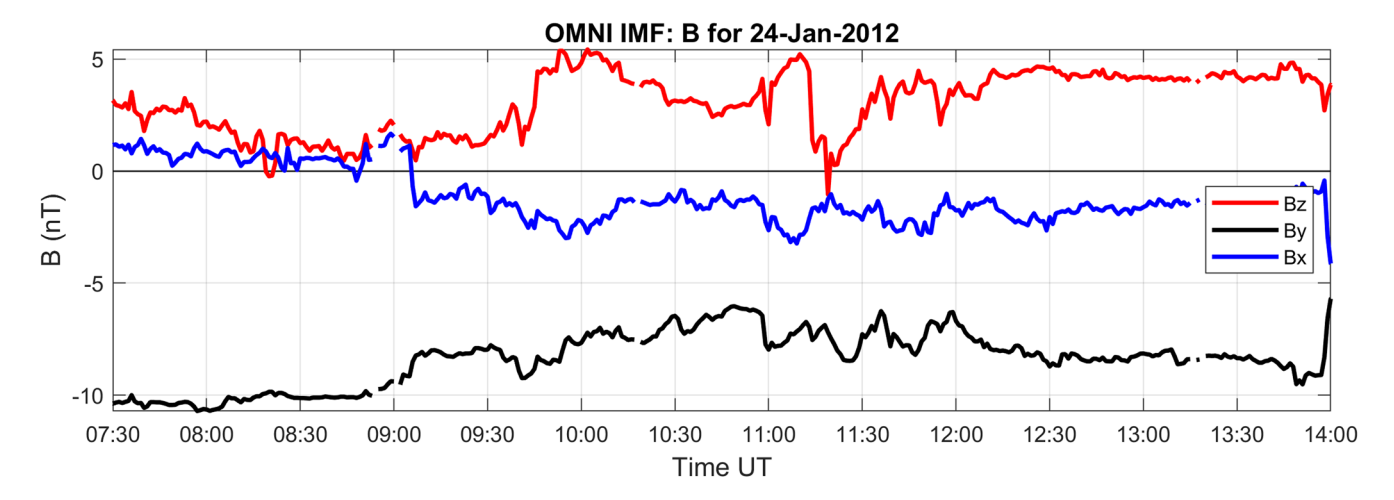


Figure 1. OMNI solar wind IMF measurements for January 24, 2012.

displayed using a 3D natural-neighbor interpolation scheme, as shown in Figure 2c (Dahlgren et al., 2012; Perry et al., 2015; Semeter et al., 2009). The interpolated data products allow flexibility in visualizing the space-time evolution of plasma. For example, plasma motion may be estimated from feature tracking as well as from the bulk Doppler shift  $(V_{LOS})$  of the received signals. It is also possible to extract cuts through the data in any direction, particularly in the direction of the magnetic field, which is nearly 90° elevation at the RISR-N location. This enables us to study plasma dynamics in the convecting frame of reference, a capabilities that will be discussed further in Section 3.1.

# 2.2. **DMSP**

The DMSP is a constellation of low-Earth orbit (LEO) sun-synchronous satellites in a dusk-dawn polar orbit at a nominal altitude of  $\sim$ 833 km. Developed primarily for weather monitoring; the DMSP spacecraft also includes a variety of plasma instruments. The orbital velocity of the DMSP satellites is  $\sim$ 7.4 km/s, which means that they cross the polar cap on a timescale similar to the timescales associated with changes in the convection pattern. Thus the spacecraft measurements contain an ambiguous mixture of spatial and temporal effects which must be partitioned using additional diagnostics. For this study, we used the thermal plasma monitor and the precipitation particle spectrometer instruments, commonly known as SSIES and SSJ/5, respectively. DMSP satellites F15 through F18 were available during the interval under study. For this study, we focus on F16 since it passed closest to RISR-N.

# 2.3. OMTI

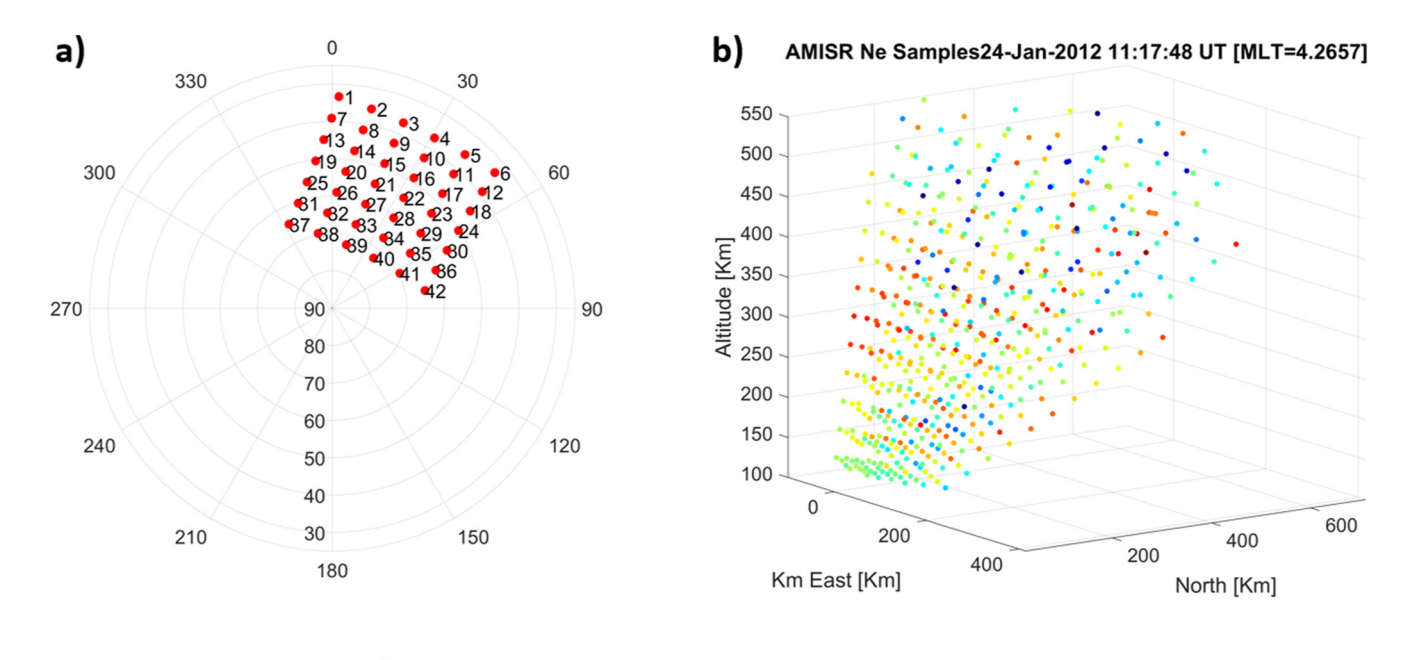
Co-located with the RISR-N facility is an all-sky imager for studying aurora and airglow. The imager is part of the OMTI managed by the Nagoya University (Shiokawa et al., 1999, 2009), and has been operational since 2005. The filters in place are for the green line (557.7 nm), red line (630 nm), thermospheric oxygen (777.4 nm), sodium line, and hydroxyl line. OMTI registers red-line images every 2 min with 30 s exposure (Hosokawa et al., 2006, 2009). In this work, the OMTI 630 nm images are used to provide space-time context to assist in the interpretation of plasma measurements by RISR-N, and orbital measurements of particles and drifts by DMSP.

# **2.4. GEMINI**

In order to better understand the time and altitude dependencies of the ionospheric responses, we shall employ a physics-based modeling. The numerical model used is the "Geospace Environment Model for Ion-Neutral Interactions" (GEMINI) based on the model described by Zettergren and Semeter (2012) and expanded by Zettergren et al. (2014, 2015) and Zettergren and Snively (2013, 2015). The model encompasses a system of fluid equations (Blelly & Schunk, 1993; Schunk, 1977) describing the ionospheric plasma utilizing the first three moments of the Boltzmann equation (mass, momentum, and energy) for each relevant species, and it is self-consistently coupled

DÍAZ PEÑA ET AL. 3 of 17





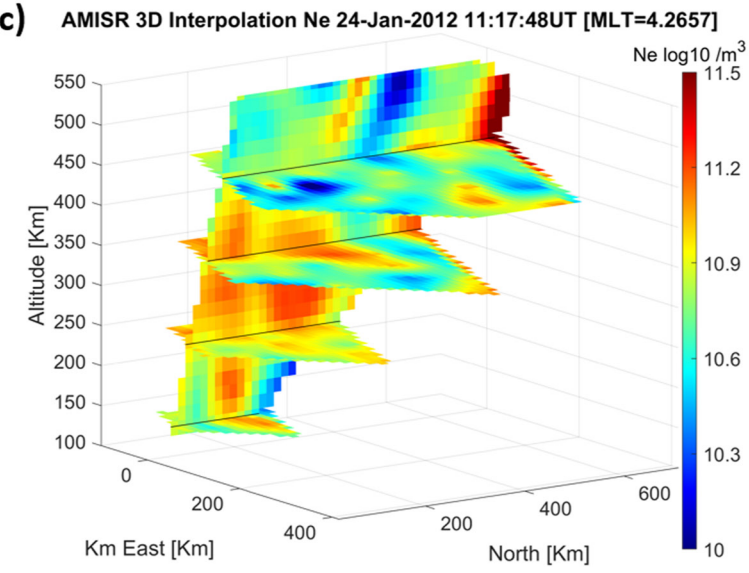


Figure 2. (a) RISR-N beam pattern in horizon coordinates for January 24, 2012, (b) Example of three-dimensional sampling acquired from this mode, (c) Example of three-dimensional interpolation product.

to an electrostatic treatment of auroral and neutral dynamo currents. The release of GEMINI used uses the first-principles suprathermal electron transport code GLOW (Solomon, 2017, and references therein) to specify auroral ionization and heating rates. The coupled GEMINI-GLOW model is a newly developed capability, as the prior version of GEMINI used a semi-empirical model of ionization.

#### 3. Observations

Our interpretation of this event is based on the combined perspective obtained from the solar wind IMF, ionospheric parameters from RISR-N, auroral morphology from OMTI, global convection using the Weimer model, and particle precipitation from DMSP. The reader is strongly encouraged to view in Supporting Information S1—in particular, Movie S1 which depicts these combined viewpoints in a single time-dependent display.

DÍAZ PEÑA ET AL. 4 of 17

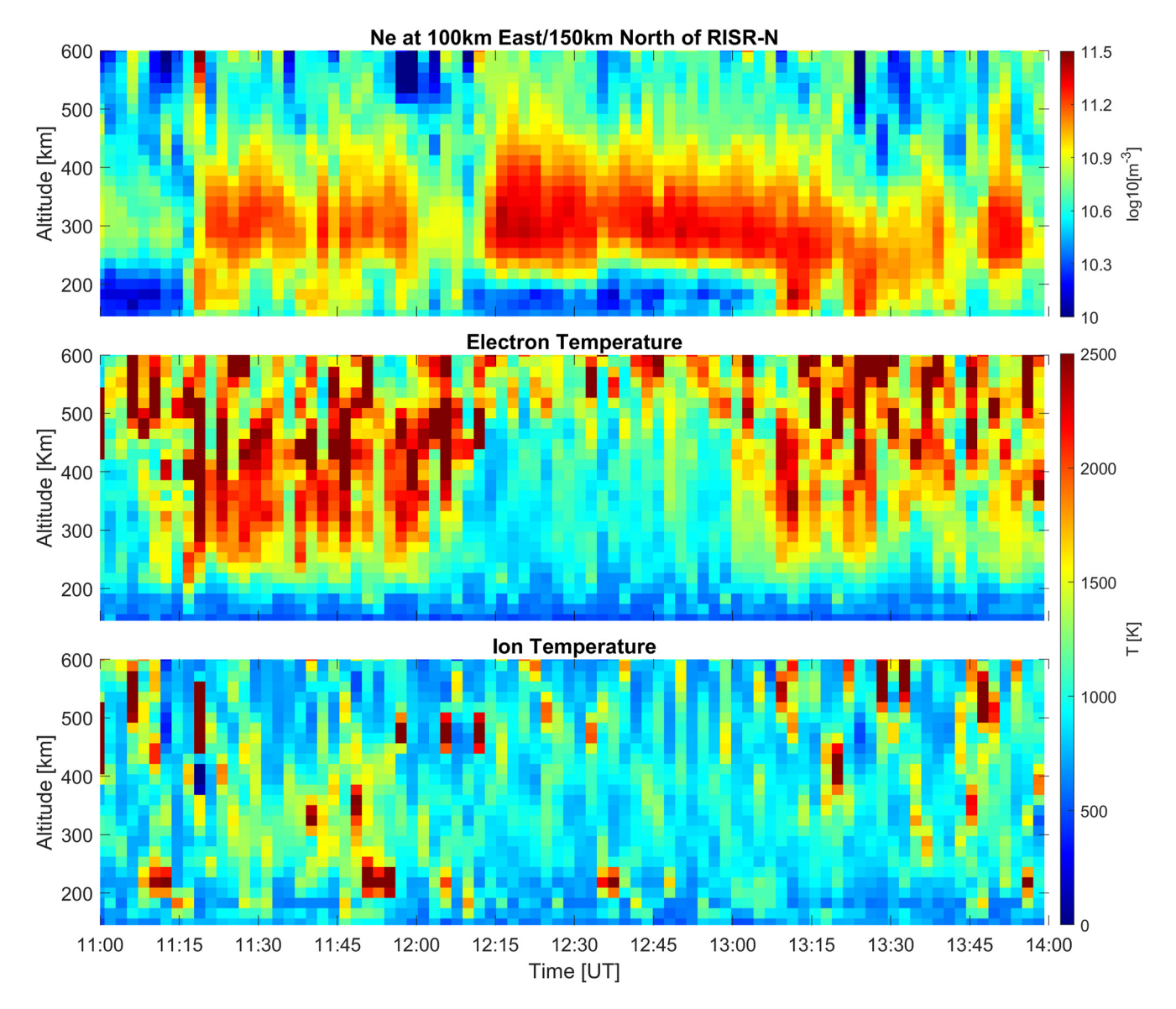


Figure 3. Time sequence of vertical profiles of  $N_e$  (top),  $T_e$  (middle), and  $T_i$  (bottom) extracted from a location 100 km east and 150 km north of RISR-N on January 24, 2012, showing intervals of correlated variations in  $N_e$  and  $T_e$  (11:20–11:58, 13:00–13:45) and an interval of uniform cold plasma enhancement (12:15–13:00).

# 3.1. RISR-N and OMTI

Figure 3 shows a time-sequence of vertical profiles of  $N_e$ ,  $T_e$ , and  $T_i$ , extracted from RISR-N during the period 11:00–14:00 UT on January 24, 2012. Evidence for plasma patches drifting through the zenith can be seen beginning at ~11:15 UT and continuing throughout this interval, all with peak density at ~300 km. The observed patches fall into two categories. From 12:15 to 13:00, the plasma appears cold and uniform in this zenith view. The IMF was steady and northward during this interval, with  $B_z = +4.5$  and  $B_y = -8$ .

By contrast, the patches between 11:20 and 11:58 UT were more structured, and correlated with high electron temperature. These structures appeared following the negative excursion in IMF  $B_z$  and the subsequent return to steady  $B_z$  north conditions (Figure 1). This class of patches has been designated "hot patch" by Zhang et al. (2017), who attributed the elevated  $T_e$  as evidence of soft auroral precipitation and, hence, conjectured that patch generation by auroral ionization and upward diffusion may be at play. This notion was updated by Ma et al. (2018), where the  $T_i/T_e$  ratio was suggested as the key to differentiating a hot patch from a classical cold patch. Ma et al. (2018) also implied that hot patches are related to precipitation and bursty flow, and represent the

DÍAZ PEÑA ET AL. 5 of 17



initial creation phase of patches that later become classical or cold patches as their temperature decreases. In this context, a cold or classical patch represents a polar cap enhanced density structure that is transported from the dayside sunlit region with dense and cold plasma (Zhang et al., 2017). The volumetric observations by RISR-N present a unique new capability for understanding the interacting mechanisms leading to the density and thermal structure of these patches, as we now discuss.

Figure 4 shows horizontal contours of  $N_e$ ,  $T_e$ , and  $T_i$  at 300 km altitude at two different times separated by  $\sim$ 13 min. The background is the corresponding 630 nm red-line image from OMTI shown in gray scale and projected at an assumed emission altitude of 230 km. The spatial coordinates indicate geographic distance east and north of RISR-N, with the location of RISR-N indicated by a yellow star at the origin. At 11:11:24 UT (panels a–c), we see spatially distinct regions of high plasma density and high electron temperature. The elevated F-region  $T_e$  is observed within the soft precipitation region, as expected, and the plasma patch is poleward of the arc boundary. By 11:24:10 UT (panels d–f), the patch has drifted across the auroral boundary, becoming co-located with the auroral heating region. The alignment of the  $T_e$  boundary with the auroral boundary in Figure 4e provides confidence in the mapping assumptions applied. This dynamic repeats for other patches in the 11:15–12:00 UT interval.

To further examine this dynamic interplay, we conducted a simultaneous analysis of horizontal and vertical cuts through the sampled volume. Figure 5 presents representations of the 3D plasma density field in contiguous 2 min intervals during the interval corresponding to Figure 4. Figures 5a-5j show horizontal cuts of  $N_e$  at 300 km altitude, as in Figure 3. The added white arrows show line-of-sight velocity vectors extracted from the bulk Doppler shift of the ISR spectrum. The vectors have been scaled by dividing by the cosine of the beam elevation angle, such that the length represents the horizontal component of the velocity toward or away from the origin of a plane at 300 km altitude (assuming velocities are predominantly horizontal—a reasonable assumption at 300 km altitude near the geomagnetic pole). Only velocity vectors with relative error <40% are included in the figure. Note that measurements meeting this threshold are coincident with regions of high plasma density, corresponding to a higher radar SNR, as expected. These vectors reveal the presence of plasma velocity components tangential and normal to the auroral boundary.

Figures 5k-5t show vertical cuts of  $N_e$  through the same interpolated volume. This view reveals the north-south motions of plasma structures at different altitudes. Of particular interest is the plasma patch centered at  $\sim 300$  km (solid ovals), and the ionization from soft precipitation extending down to  $\sim 140$  km (dashed ovals).

The patch motion is manifested in two ways in Figure 5: through direct measurements of the feature (solid ovals panels k–t), and through the bulk plasma Doppler shift (white arrows in panels (a–j)). The general southeastward motion of the patch toward the arc boundary is consistent with the line-of-sight velocities. The vectors turn strongly norhteastward (dawnward) within the arc, consistent with DMSP IDM observation (see Movie S1). The location of the particle precipitation is also revealed in two ways: through the optical imagery (background image) and through direct measurements of impact ionization (dashed ovals).

The time-sequential visualizations show that the patch trajectory had a strong equatorward component across the auroral boundary, followed by rapid dawnward motion within the arc. This behavior is consistent with the presence of a tangential reconnection electric field (de la Beaujardiere et al., 1991). Moreover, there is also a visible acceleration between 11:17UT and 11:19UT (Figures 5d–5e) where the center of the patch moves almost 100 km in a span of 2 min, which corresponds to almost 830 m/s. This is consistent with accumulating evidence that the reconnection process is universally bursty (Fear et al., 2017), including high-latitude lobe reconnection (Lockwood & Moen, 1999).

After the patch and aurora become aligned (panels f–j and p–t), it is impossible to differentiate precipitation-generated plasma from the pre-existing patch plasma in any single frame. It is only through the time-history that we can conclude that the structures observed in panel t represent a co-mingling of precipitation effects and cold plasma transport. The challenge with interpretation of such data is exacerbated by the large arc-aligned (sunward) velocities within the arc, which serve to stretch the patch along the arc, causing the F-region density enhancement to mimic the lower altitude auroral ionization pattern (e.g., panels j and t).

Further insight can be obtained by following the evolution of ionospheric parameters in the frame of reference of the advecting patch, that is, the Lagrangian reference frame. Figure 6 shows a time-sequence of vertical profiles

DÍAZ PEÑA ET AL. 6 of 17



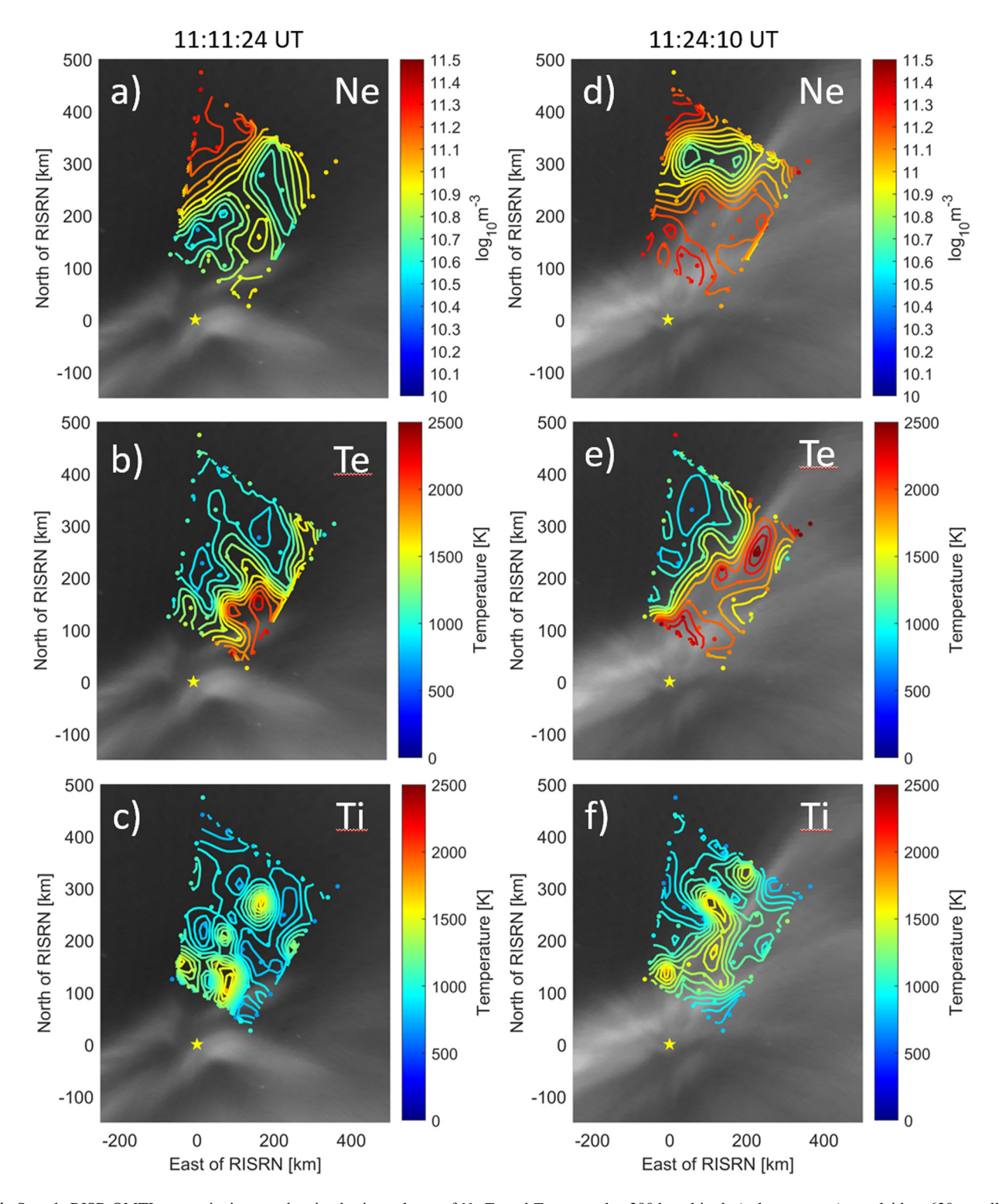


Figure 4. Sample RISR-OMTI composite images showing horizontal cuts of  $N_e$ ,  $T_e$ , and  $T_i$  extracted at 300 km altitude (color contours), overlaid on 630 nm all-sky images mapped to 230 km altitude (i.e., expected altitude of peak emission). The parameter fields are compared at two times: Panels (a–c) (11:11:24 UT) show a period with spatially separated cold patch and auroral heating; Panels (d–e) (11:24:10 UT) show a period after patch has moved across the arc boundary, creating common region of elevated  $N_e$  and  $T_e$ .

DÍAZ PEÑA ET AL. 7 of 17



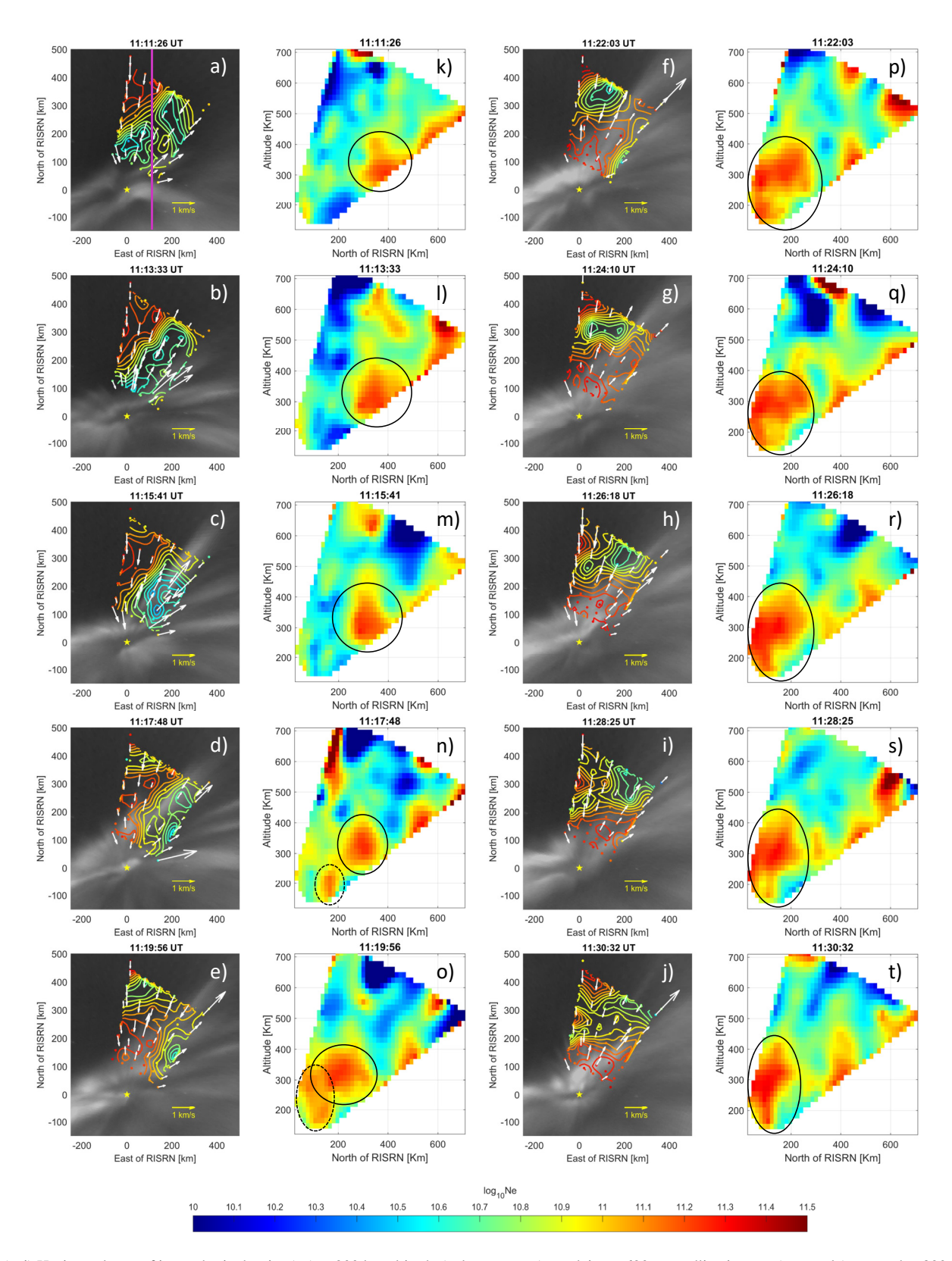


Figure 5. (a–j) Horizontal cuts of ionospheric density  $(N_e)$  at 300 km altitude (color contours) overlain on 630 nm redline images (grayscale) mapped at 230 km. White arrows represent line-of-sight velocities measured projected to a plane at 300 km altitude, as described in the text. (k–t) North-south vertical density cuts 100 km east of RISR-N represented by the pink line in (a), showing the relative motion of a plasma patch (solid ovals) and a region of plasma production by precipitation (dashed ovals). Purple line on (a) represents the location of vertical cuts.

DÍAZ PEÑA ET AL. 8 of 17

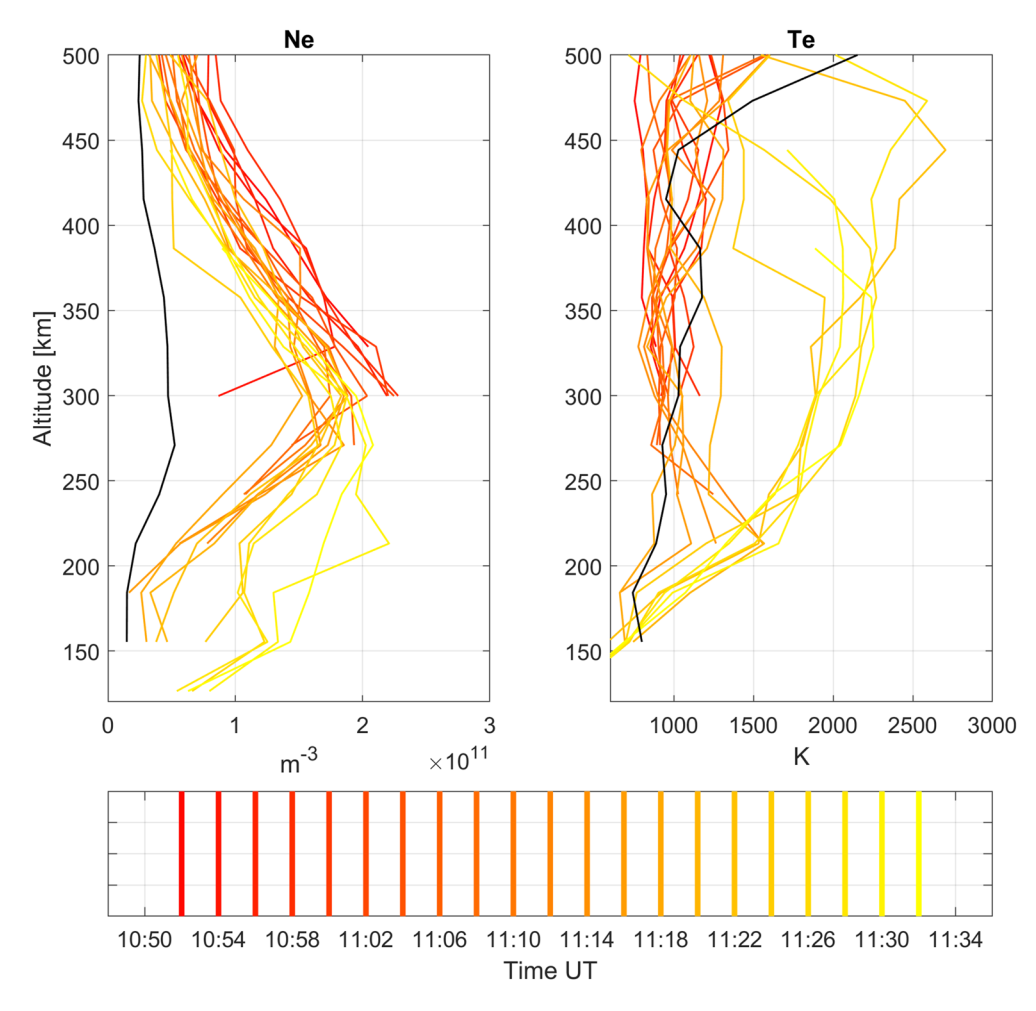


Figure 6. Altitude profiles extracted from interpolated RISR-N data that follow the center of the polar cap patch as it moves through the field of view of RISR-N. Time is indicated by color, progressing from dark red to light yellow. The black profiles represent the pre-event background conditions. The increasing ionization in the 150-250 km altitude range and the elevated  $T_e$  throughout the ionosphere are consequences of the sudden appearance of soft precipitation in the patch frame of reference. The truncated profiles are due to variations in altitude coverage within the probed volume as the structures drift through (see Figure 2).

of  $N_e$  and  $T_e$  over the interval 11:00–11:34 UT. The profiles were extracted by performing a spatial average in the horizontal direction of the parameters over the approximate area at the center of the patch. For each snapshot, the center of the patch was found, and an average was calculated over the pixels around it. The generated sequence of vertical profiles represent the average behavior in altitude. As such, the profiles illustrate how the plasma properties are evolving within the patch on average. Each profile represents a 2 min integration, and each profile is color-coded to indicate the progression of time using dark red to light yellow. The black profiles show the average quiescent background state prior to the patch event.

Figure 6 shows that  $N_e$  and  $T_e$  were relatively constant within the patch prior to encountering the region of auroral precipitation, indicated where profiles are red, with the decrease in electron density in time associated with recombination of the background ionosphere. At 11:24 UT, the patch accelerated into the region of soft precipitation, indicated where the profiles are yellow, where we see elevated F-region  $T_e$ , and a build-up of new plasma density below 250 km. These changes are consistent with the presence of an incident electron spectrum with broad energy distribution below  $\sim 300 \text{ eV}$ .

The observations provide strong evidence for a dynamic interplay between patch transport and soft auroral precipitation initiated by lobe reconnection, which resulted in a region of elevated upper F-region  $N_e$  and elevated F-region  $T_e$ . Thus, in this case, the presence of a hot patch does not indicate the initial creation of a patch, but is

DÍAZ PEÑA ET AL. 9 of 17



rather the result of a mature cold patch that has been subjected to auroral heating. The field-of-view of RISR-N is insufficient to track these dynamics further. Future studies using combined observations from RISR-N and the southward pointed RISR-C facility will certainly contribute to completing the observational picture.

#### 3.2. Global Context From OMNI and Weimer

For this particular day, the IMF  $B_y$  was consistently negative.  $B_z$  was slightly northward, except for a brief rapid transient at ~11:15 UT. By following the results of Heppner and Maynard (1987) and Potemra et al. (1984), we expect the global convection pattern to be most likely a distorted two-cell pattern. This pattern also allows for the existence of polar cap arcs as discussed by Sojka et al. (1994). No SuperDARN back scatter was available from the geographically close radars, so no SuperDARN convection map is available. We ran the Weimer model several times for this date utilizing the online CCMC tool and OMNI inputs. These Weimer models runs are empirically derived statistical electric potential maps for the high-latitude ionosphere developed by Weimer (1995) and can help us approximate the overall large-scale convection pattern. Figure 7 shows plots of Weimer equipotential contours and mapped all-sky redline images at selected times during the RISR-N experiment (see Movie S1 for the complete sequence):

- 1. 10:11 UT. Pre-event,  $B_z > 0$ ,  $B_y < 0$ . No visible aurora, model predicts dawnside cell splitting as expected for prolonged  $B_z$  north
- 2. 10:48 UT. Initial appearance of auroral activity, accompanied by continued contraction of the polar cap
- 3. 11:29 UT. First appearance of coherent the sun-aligned polar cap arc forming on the night/predawn side of the polar cap, following abrupt transition to  $B_z < 0$
- 12:48 UT. Return to steady B<sub>z</sub> north. The sun-aligned arc has become a remnant at the southern edge. Convection is small or stagnant in the vicinity of RISR-N

# 4. Discussion

The observations presented herein reveal how the combined effects of plasma transport and particle precipitation can lead to regions of elevated ionospheric density and temperature consistent with the "hot patch" designation (Zhang et al., 2017). The observations presented are consistent with the finding by Ma et al. (2018) that hot patches are more frequently observed near the polar cap boundary, whereas cold patches are more frequently observed in the central polar cap. The present study shows that both cases can result as part of a single dynamic.

Vertical parameter profiles extracted from interpolated data (Figure 3) showed multiple small-scale patches co-located with elevated electron temperature in the 11:15–12:00 UT interval and again in the 13:10–14:00 interval, with a continuous cold plasma enhancement in between. Three-dimensional time-dependent analysis showed that the F-region features were transported into the RISR-N FOV and into the regions of soft precipitation, rather than produced locally. One reason for showing both presenting both perspectives is to emphasize the importance of four-dimensional space-time observations for understanding ionospheric dynamics at geospace boundaries. The evidence is well summarized in Movie S1, which shows the combined OMNI (solar wind), RISR-N (ionosphere), OMTI (aurora), and Weimer (convection) perspectives over this interval. In what follows we discuss implications of this evidence, and employ physics-based modeling to help understand the time scales and expected signatures at LEO (e.g., DMSP).

# 4.1. Relation to Solar Wind Drivers

Figure 1 showed that during the hours preceding 11:15 UT on January 24, 2012, the IMF  $B_z$  was positive, varying between 1 and 5 nT, while  $B_y$  was negative increasing steadily (to first order) from -10 to -6 nT. The Weimer modeled convection pattern (Figure 7 and Movie S1 exhibited expected behaviors for these conditions, with a contracting dawnside convection cell and indications of bifurcation of the dawnside into smaller cells. Line-of-sight ion velocities imaged by RISR-N (Figure 5) were consistent with Weimer predictions—that is, velocities have a persistent equatorward component poleward of the auroral boundary, but a persistent sunward component equatorward of the auroral boundary. On the other hand, these velocities were not consistent with observed movements of density features in the same regions: RISR-N measured an approximately southward direction, where Weimer shows the possible existence of an eastward flow. This can be explained by two possible factors:

DÍAZ PEÑA ET AL. 10 of 17



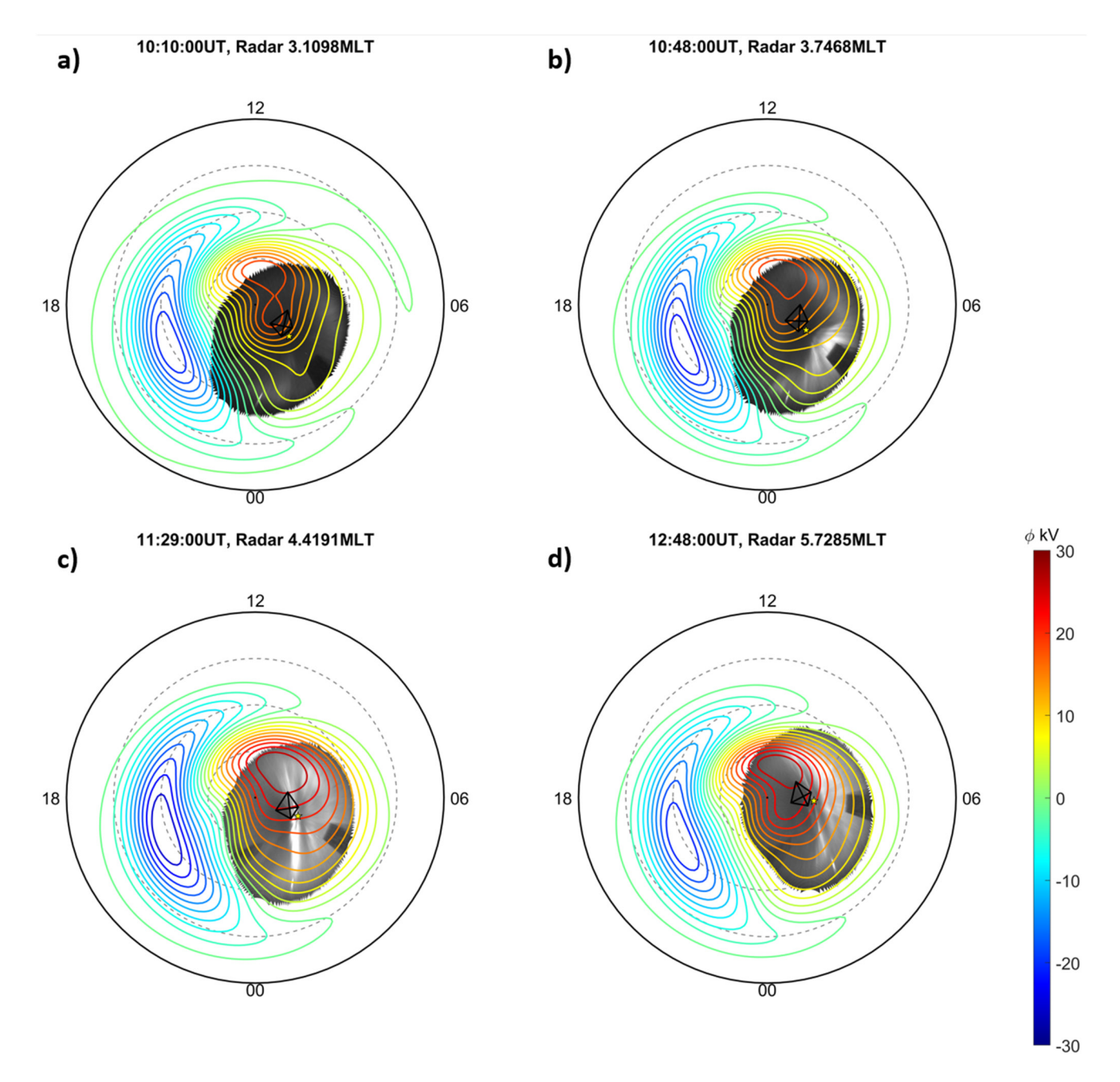


**Figure 7.** Electric potential over the polar cap from Weimer model runs, along with corresponding map-projected all-sky 630 nm images. The RISR-N location and 300 km field-of-view are indicated by the yellow star and black trapezoid, respectively.

reconnection is pushing plasma across field lines through a tangential electric field thus creating the southward movement inside a convection pattern that is exactly as Weimer presents, or since Weimer is a large scale model small scale variations are not accounted for, which is what RISR-N could be measuring in this instance.

The aurora that formed within the RISR-N FOV at ~11:07 UT in Figure 5 was characterized by dynamic rayed structures dominated by 630 nm redline emission. Mapped projections of the full all-sky field-of-view, show in Movie S1 and Figures S1–S2 in Supporting Information S1, revealed these features to comprise a sun-aligned arc. The IMF conditions for this event— $B_z > 0$ ,  $B_y < 0$ ,  $B_x > 0$ —were favorable for the formation of small-scale sun-aligned arcs (Crooker, 1986; Kullen et al., 2002). At ~11:15 UT,  $B_z$  transitioned rapidly from 5 to -1 nT. This was followed ~2 min later by a simultaneous brightening of the arc and equatorward acceleration of the patch across the precipitation boundary, as revealed by Figure 5. The rapid response of the magnetosphere-ionosphere

DÍAZ PEÑA ET AL.



system to such solar wind transients is well known, and has been investigated in observational (Ruohoniemi & Greenwald, 1998) and modeling (Lu et al., 2002) studies. The coordinated response of sun-aligned arc formation and accelerated transport across the arc boundary are the expected consequences of lobe reconnection.

#### 4.2. Role of High-Latitude Lobe Reconnection

The role of high-latitude reconnection in the formation of sun-aligned arcs has been investigated in some detail (see, Hosokawa et al., 2020, and references therein). This event meets the criteria for the tail reconnection during IMF northward non-substorm intervals (TRINNI) model proposed by Milan et al. (2005). In this model, the polar cap becomes bifurcated into two compartments, and lobe reconnection results in a transfer of flux from one polar cap compartment to another. The lifetime and migration of the resulting sun-aligned arc depends on continued lobe reconnection and  $B_y$  variations. For the present case, the negative transient in  $B_z$  at 11:15 UT is conjectured to have produced an impulsive increase in reconnection rate (see, e.g., Newell et al., 1997), which resulted in acceleration of the plasma patch into the reconnection footprint.

The creation of soft but structured precipitation from reconnection is also expected. A lobe reconnection pulse introduces free energy in the Lagrangian (plasma rest) frame in the form of magnetic tension. The energy is dissipated through the excitation of small-scale inertial Alfvén waves which accelerate electrons (e.g., Keiling, 2009, and references therein). The rayed morphology of the aurora, often observed in active polar cap arcs, is qualitatively similar to PBIs (Semeter et al., 2005) as well as auroras associated with poleward edge of a substorm expansion (Dahlgren et al., 2013), both of which are associated with Aflvénic electron acceleration. The correlation of flow bursts and particle precipitation in polar cap auroras has also been investigated directly using measurements from the FAST satellite (Bonnell et al., 1999). The four-dimensional view of the evolving ionospheric state by RISR-N provides critical evidence needed to disentangle the various processes at play.

The effects of lobe reconnection on a drifting plasma patch are best understood by tracking properties in the patch reference frame. Figure 6 shows that the ability to extract this perspective over a substantial regional volume is one advantage of an electronically scannable ISR. Figure 6 showed that the precipitation increased plasma production below 300 km, while simultaneously elevating  $T_e$  throughout the ionosphere. These effects are the expected responses to an intense flux of soft electrons ( $\lesssim$ 200 eV) associated with Alfvénic particle acceleration (Semeter & Zettergren, 2014). An important observation is that the introduction of soft precipitation did not increase the peak patch density at ~300 km. In fact, the density above 300 km can be seen to decrease slowly over time. This response is expected due to continued recombination and upward ambipolar diffusion induced by the electron heating.

#### 4.3. Numerical Modeling of Patch Formation

Investigations into the "hot patch" phenomenon have primarily rested on topside ionospheric observations by DMSP ( $\sim$ 800 km). In order to better understand how the observed dynamic below  $\sim$  400 km manifest at different altitudes, we used our observations to constrain the coupled GEMINI-GLOW model (see Section 2). Of particular interest are the effects of soft particle precipitation, which could potentially impact F-region density and topside electron heating Oksavik et al. (2006). For our present purpose, we seek to assess to what extent the observed patches could be produced by soft precipitation based on the available evidence.

The following strategy was employed. We set the initial background  $N_e$  profile to the pre-event background (no patch) in Figure 6 (black curve). We then applied an incident Maxwellian electron spectrum to the GEMINI3D upper boundary. The average energy and energy flux were initially set based on DMSP particle measurements near the auroral arc at 11:56–11:57 UT. Figure 8 shows several samples of the differential energy flux measured in the vicinity of the sun-aligned arc. The average spectrum (shown in red, with  $\sim$ 500 eV average energy) was initially applied to the model, and then adjusted to in order to best match the observed time-dependent  $T_e$  and  $N_e$  profiles observed by RISR-N. For more information on the DMSP measurements see Text S1 and Figures S1 and S2 in Supporting Information S1.

Figure 9 summarizes the results that best-matched observations (incident Maxwellian spectrum with average energy 330 eV and energy flux 0.35 mW/m²). Additional sample runs are included in Figures S3–S10 in Supporting Information S1. The source was turned on at 11:10 UT and turned off again at 11:20 UT. This duration

DÍAZ PEÑA ET AL. 12 of 17



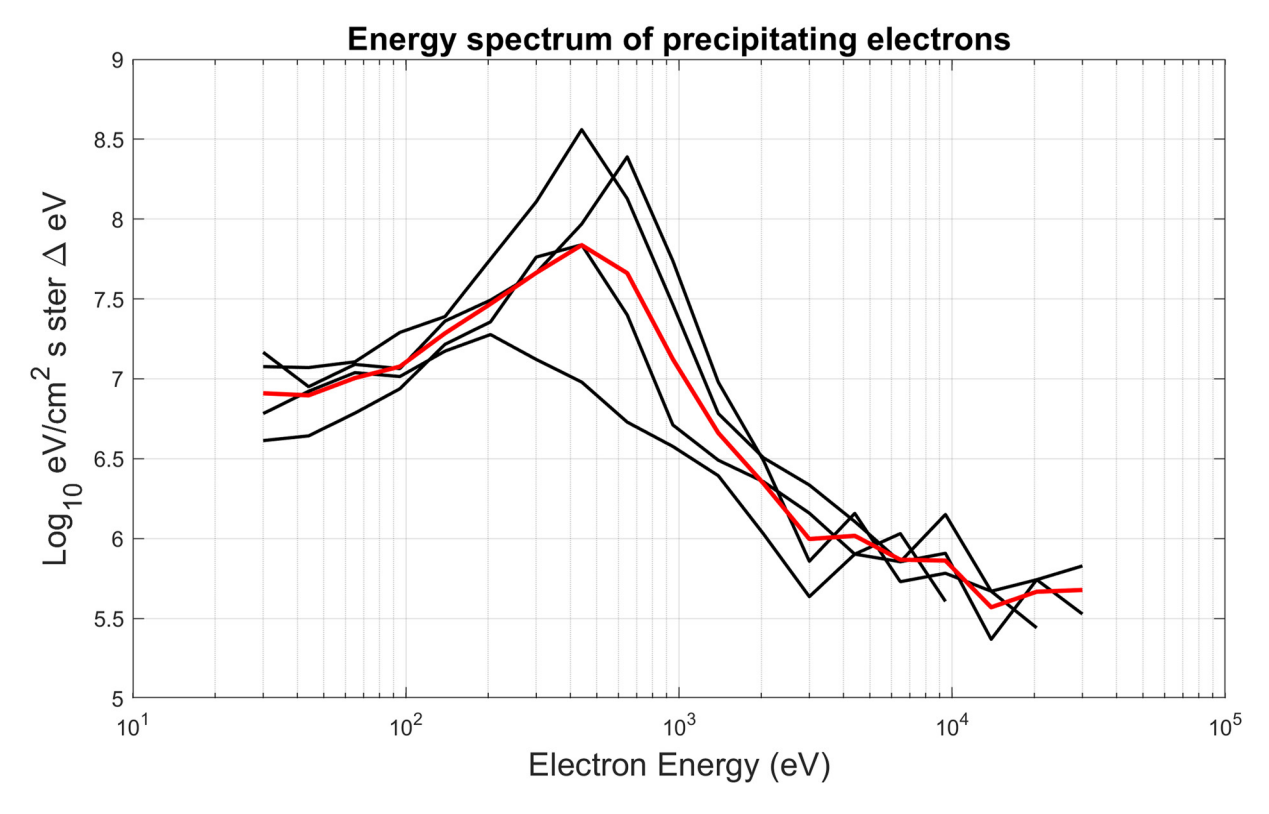


Figure 8. Energy spectrum of precipitation electrons in the area of the auroral arc. Black lines represent the measured spectrum by DMSP. Red line represents the average of such measurements.

is somewhat arbitrary, but is roughly consistent with expected residency within the sun-aligned arc, and also exceeds the time for the ionosphere to reach steady state.

Several points can be made from this run. First, the time to reach steady-state density is about 2 min at 250 km, and decreases with decreasing altitude as expected. This is consistent with observations in Figures 5 and 6, providing some confidence that we are driving the model with a plausible parameter set. Second, note that the  $T_e$  rises almost immediately at ~200 km, with higher altitudes responding somewhat more slowly. This is also consistent with observed profiles in Figure 6. This effect occurs as the result of the interplay between conduction, convection, and collisional heating by secondaries at the stopping altitude. Third, note that the plasma production for this flux is below the F-region peak at 300 km, while the  $T_e$  enhancement extends throughout the ionosphere. Thus this flux has only a minor effect on  $N_e$  at patch altitudes. These responses are expected for soft electron fluxes in the <1 keV range (Semeter & Zettergren, 2014), and are both consistent with observed behaviors (Figure 6). Lastly, after the source is removed, F-region densities return to their initial state in ~15 min. In summary, a 330 eV Mawellian with 0.35 mW/m² average flux produces the key behaviors observed in Figures 5 and 6.

Turning to the topside, at 800 km, we see that electron heating results in an increase in  $T_e$  of ~1,000 K during the application of the source. There is also an increase in  $N_e$  at this altitude that is lagged by ~4 min from the time of application of the source at 11:10 UT. Since there is no collisional production at these altitudes, the enhanced  $N_e$  is due to the upward ambipolar diffusion produced by the electron partial pressure gradient. Also, note that the  $N_e$  returns to its initial quiescent state ~7 min after the source is removed. Thus there is no long-term transportable effect produced in the topside ionosphere for this case.

Figure 9 supports the conclusion that precipitation can produce  $\sim$ 1,000 K enhancements in  $T_e$  (factor 2 above background) and order— $10^{10} \rm m^{-3}$  enhancements in  $N_e$  (factor  $\sim$ 10 above background) at 800 km DMSP altitudes, irrespective of the presence of a plasma patch in the conjugate F-region. The topside signatures observed in this event are consistent with parameters identified as a hot patch by Ma et al. (2018) and Zhang et al. (2017). Thus care must be taken when inferring lower ionospheric dynamics based on observations at DMSP altitudes. Furthermore, the presence of an F-region patch within a region of soft precipitation and enhanced  $T_e$  does not

DÍAZ PEÑA ET AL. 13 of 17



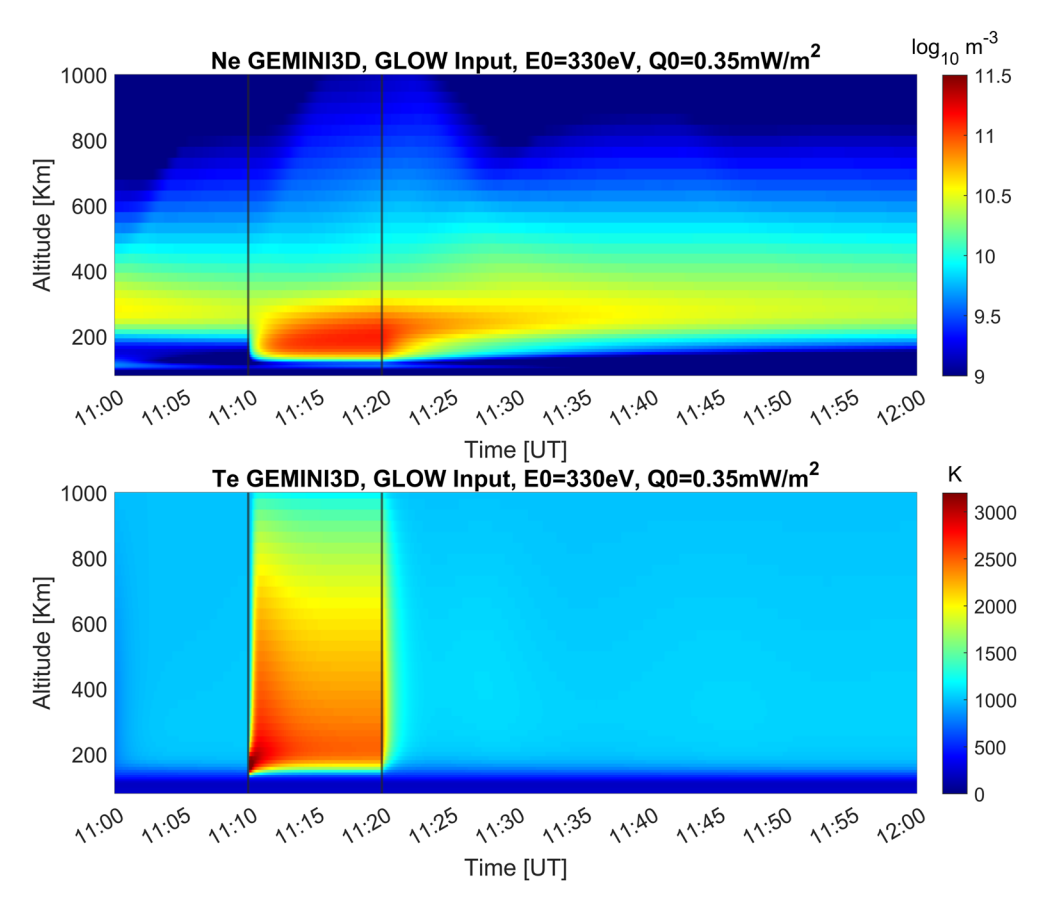


**Figure 9.** GEMINI3D run utilizing a Maxwellian spectrum for the precipitating electrons. E0 of 330 eV and energy flux of 0.35 mW/m<sup>2</sup> were used as taken from DMSP measurements closest to the arc. The time selected corresponds with the event at 11:00 UT. The range time plot was built by taking the central bin of each time step to simulate what happens right below a stream of precipitating electrons. Precipitation is turned on at exactly 11:10 UT and turned off at 11:20 UT as marked by black lines.

necessarily indicate patch production via precipitation. Transport of a cold plasma patch into a region of intensifying soft precipitation is a natural consequence of lobe reconnection, and represents an alternate mechanism by which a fully mature cold patch can become a hot patch.

#### 5. Conclusions

We have exploited the four-dimensional (space + time) imaging capabilities of the RISR-N facility to observe ionospheric dynamics in the vicinity of a high-latitude reconnection event. An isolated region of elevated electron temperature and elevated electron density can arise through a superposition of transport and precipitation effects, both natural consequences of lobe reconnection. First-principles modeling was carried out using constraints extracted from RISR-N observations in the lower ionosphere and precipitating electron spectra provided by DMSP SSJ across the polar cap during this period. The results show that the application of a 330 eV Maxwellian incident flux with 0.35 mW/m² net energy flux for a few minutes will produce signatures at 800 km that are consistent with reports of a hot patch (e.g., increase in  $T_e$  by 1,000 K, increase in  $N_e$  by factor ~10). This response is not due to impact ionization and is expected to occur irrespective of the presence a plasma patch in the conjugate F-region. The response is due primarily to upward ambipolar diffusion caused the electron heating associated with soft particle precipitation. Thus, we conclude that care must be taken when inferring lower altitude ionospheric dynamics based on in situ observations of the ambient plasma from LEO.

It is a complex and somewhat unsolved problem whether most hot patches are formed by precipitation, as opposed to being formed as cold patches that have encountered precipitation. Oksavik et al. (2006) showed how soft

DÍAZ PEÑA ET AL. 14 of 17



electron fluxes found in the cusp or the polar ionosphere can produce islands of enhanced density consistent with our accepted definition of a plasma patch, although previous research has also shown that virtually all patches come from the dayside plasma (David et al., 2016). In general time-dependent modeling is needed to link these perspectives. Examination of a more comprehensive set of events is needed to assess whether this is a common dynamic in the polar ionosphere. The study highlights the need for densely distributed measurements in space and time for understanding ionospheric dynamics in regions subject to complex forcing. The reported findings are uniquely enabled by the electronic scanning modality of the Advanced Modular ISR radars (PFISR, RISR-N, RISR-C). The forthcoming EISCAT-3D facility will build substantially upon this capability (Stamm et al., 2021).

# **Data Availability Statement**

The authors acknowledge use of NASA/GSFC's Space Physics Data Facility's OMNIWeb (or CDAWeb or ftp) service, and OMNI data. Simulation results have been provided by the Community Coordinated Modeling Center at Goddard Space Flight Center through their public Runs on Request system (http://ccmc.gsfc.nasa.gov). GEM-INI3D Version v0.14.2 archived at https://zenodo.org/record/4777372. OMTI images are available at https://doi.org/10.5281/zenodo.5550949.

# Acknowledgments References

This work was supported by the National

Science Foundation (NSF) under grant

supported by NSF Cooperative Agree-

ment 1840962 to SRI International. The

data used in this work are freely available

through the NSF-supported Open Madri-

gal Initiative (http://cedar.openmadrigal.

org/openmadrigal). Development of

GEMINI was support by NSF AGS-

1255181 and NASA NNX14AQ39G.

(APL 2.0 license); the latest source

code can be downloaded from: https://

github.com/gemini3d. The work of Y. Nishimura was supported by NASA grant

80NSSC18K0657, 80NSSC20K0604,

and 80NSSC20K0725, NSF grant AGS-

1907698, and AFOSR grant FA9559-16-

1-0364. Sponsorship of the Heliophysics

Division of the NASA Science Mission

Directorate is gratefully acknowledged.

A portion of the work was performed at

the Jet Propulsion Laboratory, California

Institute of Technology, under a contract

Shiokawa is supported by JSPS Kakenhi

with NASA. K. Hosokawa is support-

ed by JSPS Kakenhi (26302006). K.

(16H06286; 21H04518).

The GEMINI model is publicly available

ATM 1821135. RISR-N operations were

Basu, S., & Valladares, C. (1999). Global aspects of plasma structures. *Journal of Atmospheric and Solar-Terrestrial Physics*, 61(1–2), 127–139. https://doi.org/10.1016/s1364-6826(98)00122-9

Blelly, P., & Schunk, R. (1993). A comparative study of the time-dependent standard 8-, 13-and 16-moment transport formulations of the polar wind. *Annales Geophysicae*, 11(6), 443–469.

Bonnell, J., Elphic, R. C., Palfery, S., Strangeway, R. J., Peterson, W. K., Klumpar, D., et al. (1999). Observations of polar cap arcs on fast. *Journal of Geophysical Research: Space Physics*, 104(A6), 12669–12681. https://doi.org/10.1029/1999ja900085

Carlson, H. C. (1994). The dark polar ionosphere: Progress and future challenges. *Radio Science*, 29(1), 157–165. https://doi.org/10.1029/93rs02125 Carlson, H. C. (2007). Role of neutral atmospheric dynamics in cusp density and ionospheric patch formation. *Geophysical Research Letters*, 34(13). https://doi.org/10.1029/2007gl029316

Carlson, H. C. (2012). Sharpening our thinking about polar cap ionospheric patch morphology, research, and mitigation techniques. Radio Science, 47(4). https://doi.org/10.1029/2011rs004946

Coley, W., & Heelis, R. (1998). Structure and occurrence of polar ionization patches. *Journal of Geophysical Research: Space Physics*, 103(A2), 2201–2208. https://doi.org/10.1029/97ja03345

Crooker, N. U. (1986). An evolution of antiparallel merging. Geophysical Research Letters, 13(10), 1063–1066. https://doi.org/10.1029/gl013i010p01063

Crowley, G. (1996). Critical review of ionospheric patches and blobs. *Review of Radio Science*, 619–648.

Dahlgren, H., Perry, G., Semeter, J., St-Maurice, J.-P., Hosokawa, K., Nicolls, M., & Heinselman, C. (2012). Space-time variability of polar cap patches: Direct evidence for internal plasma structuring. *Journal of Geophysical Research: Space Physics*, 117(A9). https://doi.org/10.1029/2012ja017961

Dahlgren, H., Semeter, J., Marshall, R., & Zettergren, M. (2013). The optical manifestation of dispersive field-aligned bursts in auroral breakup arcs. *Journal of Geophysical Research: Space Physics*, 118(7), 4572–4582. https://doi.org/10.1002/jgra.50415

David, M., Sojka, J. J., Schunk, R., & Coster, A. (2016). Polar cap patches and the tongue of ionization: A survey of GPS TEC maps from 2009 to 2015. *Geophysical Research Letters*, 43(6), 2422–2428. https://doi.org/10.1002/2016g1068136

Davis, C., & McCrea, I. (2004). Estimating uncertainties in incoherent scatter radar parameters from random variations in time series data. *Annales Geophysicae*, 22, 3523–3529. https://doi.org/10.5194/angeo-22-3523-2004

de la Beaujardiere, O., Lyons, L., & Friis-Christensen, E. (1991). Sondrestrom radar measurements of the reconnection electric field. *Journal of Geophysical Research: Space Physics*, 96(A813), 907912–907913. https://doi.org/10.1029/91ja01174

De la Beaujardiere, O., Lyons, L., Ruohoniemi, J., Friis-Christensen, E., Danielsen, C., Rich, F., & Newell, P. (1994). Quiet-time intensifications along the poleward auroral boundary near midnight. *Journal of Geophysical Research: Space Physics*, 99(A1), 287–298. https://doi.org/10.1029/93ja01947

Dungey, J. W. (1961). Interplanetary magnetic field and the auroral zones. *Physical Review Letters*, 6(2), 47–48. https://doi.org/10.1103/physrevlett.6.47

Farley, D. T. (1969). Incoherent scatter correlation function measurements. *Radio Science*, 4, 935–953. https://doi.org/10.1029/RS004i010p00935
Fear, R. C., Trenchi, L., Coxon, J., & Milan, S. E. (2017). How much flux does a flux transfer event transfer? *Journal of Geophysical Research:*Space Physics, 122(12), 12–310. https://doi.org/10.1002/2017ja024730

Fuselier, S., Petrinec, S., & Trattner, K. (2000). Stability of the high-latitude reconnection site for steady northward IMF. Geophysical Research Letters, 27(4), 473–476. https://doi.org/10.1029/1999gl003706

Gosling, J. T., Thomsen, M. F., Bame, S. J., Elphic, R. C., & Russell, C. T. (1991). Observations of reconnection of interplanetary and lobe magnetic field lines at the high-latitude magnetopause. *Journal of Geophysical Research: Space Physics*, 96(A8), 14097–14106. https://doi. org/10.1029/91JA01139

Heppner, J., & Maynard, N. (1987). Empirical high-latitude electric field models. *Journal of Geophysical Research: Space Physics*, 92(A5), 4467–4489. https://doi.org/10.1029/ja092ia05p04467

Hosokawa, K., Kashimoto, T., Suzuki, S., Shiokawa, K., Otsuka, Y., & Ogawa, T. (2009). Motion of polar cap patches: A statistical study with all-sky airglow imager at resolute bay, Canada. *Journal of Geophysical Research: Space Physics*, 114(A4). https://doi.org/10.1029/2008ja014020
 Hosokawa, K., Kullen, A., Milan, S., Reidy, J., Zou, Y., Frey, H. U., et al. (2020). Aurora in the polar cap: A review. *Space Science Reviews*, 216(1), 15. https://doi.org/10.1007/s11214-020-0637-3

DÍAZ PEÑA ET AL. 15 of 17



- Hosokawa, K., Shiokawa, K., Otsuka, Y., Nakajima, A., Ogawa, T., & Kelly, J. (2006). Estimating drift velocity of polar cap patches with all-sky airglow imager at resolute bay, Canada. *Geophysical Research Letters*, 33(15). https://doi.org/10.1029/2006gl026916
- Keiling, A. (2009). Alfvén waves and their roles in the dynamics of the Earth's magnetotail: A review. Space Science Reviews, 142(1-4), 73-156. https://doi.org/10.1007/s11214-008-9463-8
- Kullen, A., Brittnacher, M., Cumnock, J. A., & Blomberg, L. G. (2002). Solar wind dependence of the occurrence and motion of polar auroral arcs: A statistical study. *Journal of Geophysical Research*, 107(A11), 1362. https://doi.org/10.1029/2002JA009245
- Lockwood, M., & Carlson, H. (1992). Production of polar cap electron density patches by transient magnetopause reconnection. *Geophysical Research Letters*, 19(17), 1731–1734. https://doi.org/10.1029/92gl01993
- Lockwood, M., & Moen, J. (1999). Reconfiguration and closure of lobe flux by reconnection during northward IMF: Possible evidence for signatures in cusp/cleft auroral emissions. *Annales Geophysicae*, 17(8), 996–1011. https://doi.org/10.1007/s00585-999-0996-2
- Lu, G., Holzer, T. E., Lummerzheim, D., Ruohoniemi, J. M., Stauning, P., Troshichev, O., & Parks, G. (2002). Ionospheric response to the interplanetary magnetic field southward turning: Fast onset and slow reconfiguration. *Journal of Geophysical Research: Space Physics*, 107(A8). https://doi.org/10.1029/2001ja000324
- Ma, Y.-Z., Zhang, Q.-H., Xing, Z.-Y., Heelis, R. A., Oksavik, K., & Wang, Y. (2018). The ion/electron temperature characteristics of polar cap classical and hot patches and their influence on ion upflow. Geophysical Research Letters, 45(16), 8072–8080. https://doi.org/10.1029/2018gl079099
- McEwen, D., & Harris, D. (1996). Occurrence patterns of F layer patches over the north magnetic pole. *Radio Science*, 31(3), 619–628. https://doi.org/10.1029/96rs00312
- Milan, S. E., Hubert, B., & Grocott, A. (2005). Formation and motion of a transpolar arc in response to dayside and nightside reconnection. Journal of Geophysical Research, 110(A1), A01212. https://doi.org/10.1029/2004JA010835
- Newell, P. T., Xu, D., Meng, C.-I., & Kivelson, M. G. (1997). Dynamical polar cap: A unifying approach. *Journal of Geophysical Research: Space Physics*, 102(A1), 127–139. https://doi.org/10.1029/96JA03045
- Øieroset, M., Sandholt, P., Denig, W., & Cowley, S. (1997). Northward interplanetary magnetic field cusp aurora and high-latitude magnetopause reconnection. *Journal of Geophysical Research: Space Physics*, 102(A6), 11349–11362. https://doi.org/10.1029/97ja00559
- Oksavik, K., Moen, J., & Carlson, H. C. (2004). High-resolution observations of the small-scale flow pattern associated with a poleward moving auroral form in the cusp. *Geophysical Research Letters*, 31(11), L11807. https://doi.org/10.1029/2004GL019838
- Oksavik, K., Ruohoniemi, J., Greenwald, R., Baker, J., Moen, J., Carlson, H., & Lester, M. (2006). Observations of isolated polar cap patches by the European incoherent scatter (EISCAT) Svalbard and super dual auroral radar network (SuperDARN) Finland radars. *Journal of Geophysical Research: Space Physics*, 111(A5). https://doi.org/10.1029/2005ja011400
- Onsager, T., Scudder, J., Lockwood, M., & Russell, C. (2001). Reconnection at the high-latitude magnetopause during northward interplanetary magnetic field conditions. *Journal of Geophysical Research: Space Physics*, 106(A11), 25467–25488. https://doi.org/10.1029/2000ja000444
- Perry, G., Dahlgren, H., Nicolls, M., Zettergren, M., St-Maurice, J.-P., Semeter, J., et al. (2015). Spatiotemporally resolved electrodynamic properties of a sun-aligned arc over resolute bay. *Journal of Geophysical Research: Space Physics*, 120(11), 9977–9987. https://doi.org/10.1002/2015ja021790
- Potemra, T., Zanetti, L., Bythrow, P., Lui, A., & Iijima, T. (1984). By-dependent convection patterns during northward interplanetary magnetic field. *Journal of Geophysical Research: Space Physics*, 89(A11), 9753–9760. https://doi.org/10.1029/ja089ia11p09753
- Ruohoniemi, J. M., & Greenwald, R. A. (1998). The response of high-latitude convection to a sudden southward IMF turning. Geophysical Research Letters, 25(15), 2913–2916. https://doi.org/10.1029/98GL02212
- Schunk, R. (1977). Mathematical structure of transport equations for multispecies flows. Reviews of Geophysics, 15(4), 429–445. https://doi.org/10.1029/rg015i004p00429
- Semeter, J., Butler, T., Heinselman, C., Nicolls, M., Kelly, J., & Hampton, D. (2009). Volumetric imaging of the auroral ionosphere: Initial results from PFISR. *Journal of Atmospheric and Solar-Terrestrial Physics*, 71(6–7), 738–743. https://doi.org/10.1016/j.jastp.2008.08.014
- Semeter, J., Heinselman, C., Sivjee, G., Frey, H., & Bonnell, J. (2005). Ionospheric response to wave-accelerated electrons at the poleward auroral boundary. *Journal of Geophysical Research*, 110(A9), 11310. https://doi.org/10.1029/2005JA011226
- Semeter, J., Heinselman, C. J., Thayer, J. P., Doe, R. A., & Frey, H. U. (2003). Ion upflow enhanced by drifting F-region plasma structure along the nightside polar cap boundary. *Geophysical Research Letters*, 30, 3–1. https://doi.org/10.1029/2003GL017747
- Semeter, J., & Zettergren, M. (2014). Model-based inversion of auroral processes. In J. Huba, R. Schunk, & G. Khazanov (Eds.), Modeling the ionosphere-thermosphere system (pp. 309–321). John Wiley & Sons, Ltd. https://doi.org/10.1002/9781118704417.ch25
- Shiokawa, K., Katoh, Y., Satoh, M., Ejiri, M., Ogawa, T., Nakamura, T., & Wiens, R. (1999). Development of optical mesosphere thermosphere imagers (OMTI). Earth Planets and Space, 51(7–8), 887–896. https://doi.org/10.1186/bf03353247
- Shiokawa, K., Otsuka, Y., & Ogawa, T. (2009). Propagation characteristics of nighttime mesospheric and thermospheric waves observed by Optical Mesosphere Thermosphere Imagers at middle and low latitudes. Earth Planets and Space, 61(4), 479–491. https://doi.org/10.1186/ bf03353165
- Sojka, J. J., Zhu, L., Crain, D., & Schunk, R. W. (1994). Effect of high-latitude ionospheric convection on sun-aligned polar caps. *Journal of Geophysical Research: Space Physics*, 99(A5), 8851–8863. https://doi.org/10.1029/93ja02667
- Solomon, S. C. (2017). Global modeling of thermospheric airglow in the far ultraviolet. Journal of Geophysical Research: Space Physics, 122(7), 7834–7848. https://doi.org/10.1002/2017ja024314
- Stamm, J., Vierinen, J., Urco, J. M., Gustavsson, B., & Chau, J. L. (2021). Radar imaging with EISCAT 3D. Annales Geophysicae, 39(1), 119–134. https://doi.org/10.5194/angeo-39-119-2021
- Strangeway, R. J., Russell, C. T., Carlson, C. W., McFadden, J. P., Ergun, R. E., Temerin, M., et al. (2000). Cusp field-aligned currents and ion outflows. *Journal of Geophysical Research: Space Physics*, 105(A9), 21129–21141. https://doi.org/10.1029/2000ja900032
- Tsunoda, R. T. (1988). High-latitude F region irregularities: A review and synthesis. Reviews of Geophysics, 26(4), 719–760. https://doi.org/10.1029/rg026i004p00719
- Valladares, C., Decker, D., Sheehan, R., Anderson, D., Bullett, T., & Reinisch, B. (1998). Formation of polar cap patches associated with north-to-south transitions of the interplanetary magnetic field. *Journal of Geophysical Research: Space Physics*, 103(A7), 14657–14670. https://doi.org/10.1029/97ja03682
- Watanabe, M., Kabin, K., Sofko, G. J., Rankin, R., Gombosi, T. I., Ridley, A. J., & Clauer, C. R. (2005). Internal reconnection for northward interplanetary magnetic field. *Journal of Geophysical Research: Space Physics*, 110(A6). https://doi.org/10.1029/2004ja010832
- Weimer, D. (1995). Models of high-latitude electric potentials derived with a least error fit of spherical harmonic coefficients. *Journal of Geo*physical Research: Space Physics, 100(A10), 19595–19607. https://doi.org/10.1029/95ja01755
- Zettergren, M., Lynch, K., Hampton, D., Nicolls, M., Wright, B., Conde, M., et al. (2014). Auroral ionospheric F region density cavity formation and evolution: Mica campaign results. *Journal of Geophysical Research: Space Physics*, 119(4), 3162–3178. https://doi.org/10.1002/2013ja019583

DÍAZ PEÑA ET AL. 16 of 17



- Zettergren, M., & Semeter, J. (2012). Ionospheric plasma transport and loss in auroral downward current regions. *Journal of Geophysical Research: Space Physics*, 117(A6). https://doi.org/10.1029/2012ja017637
- Zettergren, M., Semeter, J., & Dahlgren, H. (2015). Dynamics of density cavities generated by frictional heating: Formation, distortion, and instability. *Geophysical Research Letters*, 42(23), 10–120. https://doi.org/10.1002/2015gl066806
- Zettergren, M., & Snively, J. (2013). Ionospheric signatures of acoustic waves generated by transient tropospheric forcing. *Geophysical Research Letters*, 40(20), 5345–5349. https://doi.org/10.1002/2013gl058018
- Zettergren, M., & Snively, J. (2015). Ionospheric response to infrasonic-acoustic waves generated by natural hazard events. *Journal of Geophysical Research: Space Physics*, 120(9), 8002–8024. https://doi.org/10.1002/2015ja021116
- Zhang, Q.-H., Ma, Y.-Z., Jayachandran, P., Moen, J., Lockwood, M., Zhang, Y.-L., et al. (2017). Polar cap hot patches: Enhanced density structures different from the classical patches in the ionosphere. *Geophysical Research Letters*, 44(16), 8159–8167. https://doi.org/10.1002/2017g1073439
- Zhang, Q.-H., Moen, J., Lockwood, M., McCrea, I., Zhang, B.-C., McWilliams, K. A., et al. (2016). Polar cap patch transportation beyond the classic scenario. *Journal of Geophysical Research: Space Physics*, 121(9), 9063–9074. https://doi.org/10.1002/2016ja022443
- Zou, Y., Nishimura, Y., Burchill, J. K., Knudsen, D. J., Lyons, L. R., Shiokawa, K., et al. (2016). Localized field-aligned currents in the polar cap associated with airglow patches. *Journal of Geophysical Research: Space Physics*, 121(10), 10–172. https://doi.org/10.1002/2016ja022665
- Zou, Y., Nishimura, Y., Lyons, L. R., Shiokawa, K., Donovan, E. F., Ruohoniemi, J. M., et al. (2015). Localized polar cap flow enhancement tracing using airglow patches: Statistical properties, IMF dependence, and contribution to polar cap convection. *Journal of Geophysical Research: Space Physics*, 120(5), 4064–4078. https://doi.org/10.1002/2014ja020946

DÍAZ PEÑA ET AL. 17 of 17